ADVANCED OPTICAL MATERIALS
www.advopticalmat.de

Filaments for 3D Printing of Iridescent Structural Colors

*Lukas Siegwardt, Georg Hemkemeier, and Markus Gallei**

Inspired by nature, this work presents a scalable method to produce opalescent 3D printing filaments with angle-dependent structural color. Compared to conventional colorants, these colors provide a more vivid appearance, possess the ability to dynamically change in response to alterations of illumination, and may feature superior longevity as well as durability. Particle synthesis via emulsion polymerization in starved-feed mode is utilized to achieve a tailored core–shell particle architecture. During processing, the thermoplastic polyacrylate-based shells form a continuous matrix, wherein the pristine polystyrene cores self-assemble. The colloidal ordered structure thus formed selectively scatters light according to Bragg's law. Adjusting particle size makes the perceived colors easily tunable over the visible spectrum. The filaments are printable on entry-level printers with comparable settings to commercial filaments and state-of-the-art print quality. With this work, sustainable 3D printing of iridescent objects with a novel and superior coloration strategy becomes possible for everyone – from hobbyists over customized goods and industrial prototypes to serial production.

1. Introduction

3D printing technologies are of increasingimportance and have created a flexible design for various materials in the last decade, experiencing exponential growth in academic interest and industrial production capacity. Fused deposition modeling (FDM) is one of the most common techniques among all printing methods with broad commercialization. FDM printers continuously melt, extrude, and deposit a thermoplastic filament, which cools down and solidifies on the printing bed to build a 3D object layer by layer. FDM offers several advantages, such as convenient customizability, short lead times, the possibility to endow devices with complex geometries and functionalities of precisely prescribed microarchitectures, as well as high material- and cost-efficiency. It is widely used, from low-budget printers for hobbyists and designers to industrial rapid prototyping and large-scale serial production.[1]

As in most polymers and plastics, coloration of FDM filaments is achieved by adding pigments or dye. These are, however, prone to photobleaching, can be washed out, and some contain toxic or otherwise harmful ingredients. Meanwhile, structural colors in nature overcome these disadvantages with an intricate structural design on the nanoscale in terms of light scattering on periodic alterations of the refractive index. Natural organisms utilize structural colors for camouflage, communication, warning, and other purposes. They enable a more vivid and often iridescent appearance, which can be observed in peacocks, butterflies, or opal gemstones. Another advantage is their dynamic switching capability, as utilized by chameleons.[2]

Given the allure of advantages, the quest to reproduce bioinspired structural color synthetically has gained significant interest. A variety of processing techniques have been explored, including colloidal (self-)assembly, spin- or spray-coating, lithography, drying methods, layer-by-layer deposition, and shear-alignment techniques. Furthermore, supramolecular photonic structures based on polymers, liquid crystals, and colloids have been successfully fabricated. However, the majority of these methods are not suitable for large-scale industrial applications due to their limitations in 2D structures and/or scalability.[2b,g,3] Within the last decade, several 3D printing approaches to produce geometrically complex objects with structural color have been reported, as recently reviewed by several authors.[3b,4] Commonly used 3D printing techniques for structural color include, among others, inkjet printing and direct-ink-writing (DIW) techniques[5] or photopolymerization approaches.[6] FDM fundamentally differs from these techniques, as it relies on the use of a thermoplastic filament instead of, for example, ink, resin, or powder. Although FDM has become one of the most studied 3D printing techniques for polymers with advanced properties and novel functionalities,[4b,7] filaments with iridescent structural color have not yet been produced with scalable methods, and reports on the topic are scarce.[8]

Thus, there is a need for FDM filaments with tunable structural colors that are printable with state-of-the-art resolution and object complexity on commercial printers. This work aims to

L. Siegwardt, G. Hemkemeier, M. Gallei
Polymer Chemistry
Saarland University
Campus C42, 66123 Saarbrücken, Germany
E-mail: markus.gallei@uni-saarland.de
M. Gallei
Saarene
Saarland Center for Energy Materials and Sustainability
Campus C42, 66123 Saarbrücken, Germany

The ORCID identification number(s) for the author(s) of this article can be found under https://doi.org/10.1002/adom.202401703

DOI: 10.1002/adom.202401703

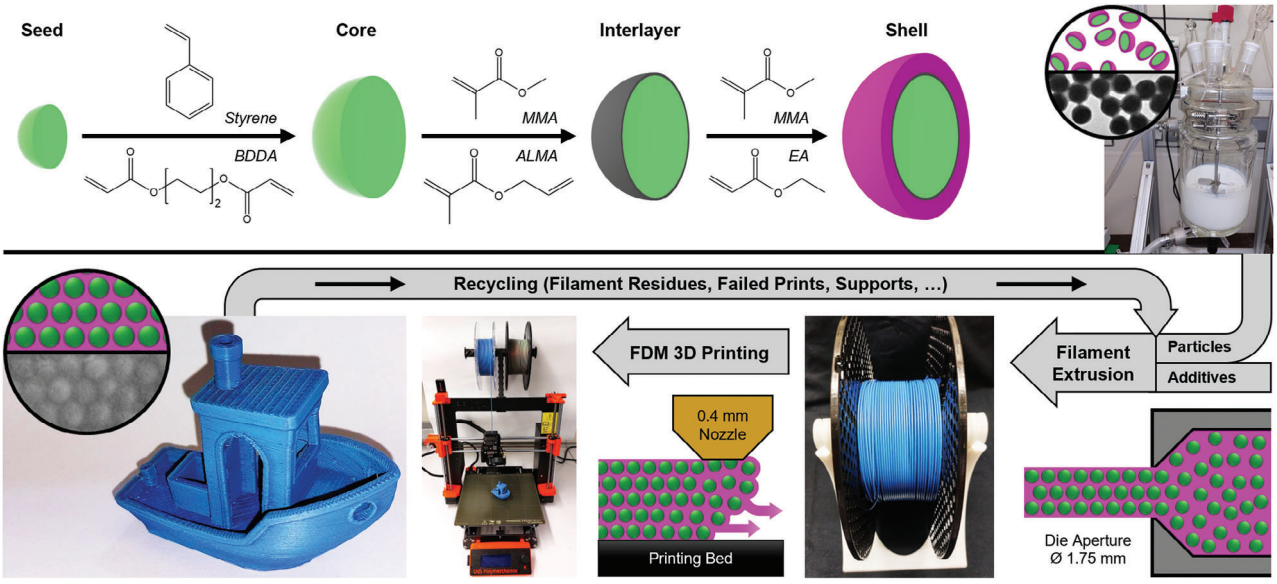

Figure 1. Scheme of the particle synthesis via stepwise emulsion polymerization (top) and subsequent processing steps (bottom). After synthesis, the obtained particles are freeze–dried and mixed with additives. During filament extrusion and 3D printing, the particles are exposed to elevated temperatures, causing the thermoplastic shell polymer to form a continuous phase. The dimensionally stable cores self-assemble inside this fluid matrix, which gives rise to the iridescent structural color. 3D printed objects and residues can be re-extruded to a recycled filament without quality deterioration or processing alterations. Digital STL model of the #3DBenchy used under terms of the CC BY-ND 4.0 license.[18] Copyright 2015, CreativeTools.

provide such filaments using the promising core–shell particle (CSP) architecture. CSP for structural color materials can be based on inorganic, organic, or hybrid materials.[5c,9] Polymeric CSP are prepared via stepwise emulsion polymerization protocols. The pristine cores usually consist of cross-linked polystyrene, whereas polyacrylates are often used to form a soft, immobilized shell. Core and shell must be covalently connected via a thin interlayer, which ensures processing stability by preventing detachments of shell polymer and phase separation. During processing at elevated temperatures, the shell polymer chains of separate particles form a continuous and viscous phase. Driven by shear forces, the dimensionally stable cores self-assemble inside this matrix to form a close-packed lattice structure.[10]

CSP ordered in this fashion are 3D photonic crystals. The periodic change in the refractive index between the crystalline core lattice and the surrounding shell matrix causes selective light scattering. Bragg's law of diffraction states that the reflected color is proportional to the lattice constant and correlates directly with the particle diameter. Since diameters are conveniently tunable from 100 to 500 nm, every color within the visible spectrum (and somewhat beyond) can be achieved. The reflected color also depends on the angle of view and light incidence, facilitating an iridescent and shimmering appearance.[10d,11] Additionally, stimuli-responsive (co)polymers can be incorporated into the shell material. This enables a reversible visual change upon application of external triggers, such as pH-value,[12] redox chemistry,[9b,13] solvents,[14] light,[15] or temperature.[14a,15a] The advanced optics and tunable rheo-mechanical properties of CSP enable various applications for smart sensing and monitoring, anti-counterfeiting, or functional optical devices with dynamic switchability.[2b,3c,16]

The inherent ability of CSP to self-assemble into a photonic crystal is utilized in various processing techniques. One of the most common methods is melt-shearing, essentially a uniaxial pressing at elevated temperatures. Thereby, free-standing and crack-free films can be prepared.[10d,e,17] By combining extrusion and oscillatory shearing, foils with lengths of several meters are accessible.[3a,10a,b] Both methods are suitable for large-scale industrial production but are limited to thin 2D films and foils. Recently, small amounts (≤5 g) of CSP have been 3D printed on a custom-built DIW printer by our group.[5b,c] Due to the elastomeric nature of the shell polymer, printed objects were viscoelastic at room temperature and showed mechanochromic properties. Filament-based printing – which requires a thermoplastic material – has not been realized, and no other scalable method for large-scale 3D bulk structures is available yet.[3b,5c] In this work, the state-of-the-art particle architecture of CSP is altered, customized synthesis and processing techniques are developed, and tailored additives are incorporated. Thus, the appropriate mechanical, rheological, and thermal properties for FDM are achieved, which differ fundamentally from the required properties for state-of-the-art processing methods, such as melt-shearing, foil extrusion, or DIW. The filaments are available in all colors of the rainbow and do not require high-end or customized 3D printers but can be printed on entry-level FDM machines with comparable quality to commercial filaments.

2. Results and Discussion

2.1. Particle Synthesis

The preparation of structural color filaments for 3D printing involved several steps, as summarized in **Figure 1**. Particle synthesis was followed by freeze–drying, mixing with additives, and filament extrusion. The filaments thus obtained were printed with high resolution and a level of detail comparable to commercial

Table 1. Particle diameters of all core batches and CSP.

Batch	CSP1	CSP2	CSP3	CSP4	CSP5	CSP6	CSP7
D_{TEM} Core [nm]	146 ± 6	159 ± 7	169 ± 8	180 ± 5	195 ± 8	207 ± 8	217 ± 9
D_{DLS} Core [nm]	149 PDI 0.02	159 PDI 0.03	172 PDI 0.02	182 PDI 0.03	198 PDI 0.04	208 PDI 0.04	231 PDI 0.03
D_{TEM} CSP [nm]	197 ± 8	209 ± 9	230 ± 11	242 ± 7	262 ± 8	269 ± 8	280 ± 9
D_{DLS} CSP [nm]	204 PDI 0.03	226 PDI 0.02	248 PDI 0.03	252 PDI 0.02	275 PDI 0.03	286 PDI 0.04	305 PDI 0.05

filaments. While filament extrusion, subsequent 3D printing, and arrangement of the particles into a photonic crystal will be discussed in the following chapters, this section focuses on the first and most crucial step: particle synthesis.

The CSP synthesis was conducted via stepwise emulsion polymerization. First, a batch polymerization of poly(styrene-*co*-butanediol diacrylate) (P(S-*co*-BDDA)) was done to obtain seed particles. Afterward, the seeds were steadily grown to the desired size by dropwise addition of styrene and BDDA as monomers in starved-feed mode. PS was chosen as the core material due to its high refractive index of 1.59, compared to the polyacrylate-based shell with 1.48. Thus, a high refractive index contrast between the core and shell was obtained, an essential prerequisite for structural color.[10d,11] BDDA was used as a cross-linking agent. The high cross-linking density hindered diffusion into the core particles and thus prevented mixing with the shell during synthesis and subsequent processing. Moreover, it is well known from the literature that PS particles, cross-linked in this fashion, keep their round shape above the glass transition and under shear forces.[5b,c,11b,19] Thus, the dimensional stability of the cores during processing via filament extrusion and 3D printing was ensured.

The starved-feed mode allowed for high control over the polymerization and enabled the preparation of core particles with tailored sizes. As will be discussed in more detail in the following chapters, smaller particles generally reflect shorter wavelengths, for example, blue light. In contrast, longer wavelengths (such as green or red light) require larger particles. Two strategies controlled the core particle size. First, the surfactant concentration in the seed stage was varied. The more surfactant was used, the more seed particles were formed. At given monomer content, more growing particles resulted in smaller sizes. Second, the monomer concentration in starved-feed mode was varied. The more monomer was added, the longer the particles grew, ultimately leading to larger sizes.

Overall, seven batches of core particles C1-7 were prepared, which exclusively differed in particle size. The average particle diameters and size distributions were determined by dynamic light scattering (DLS) and transmission electron microscopy (TEM), as summarized in **Table 1**. Both methods showed that particles with well-defined sizes were obtained for all batches and that particle size continuously increased from C1 to C7. Exemplary measurements for C1 and C7 are shown in **Figure 2**, whereas the DLS and TEM measurements for C2 to C6 are depicted in the Supporting Information (Figure S1, Supporting Information). The hydrodynamic diameters D_{DLS} describe the particles dispersed in water and thus in a swollen state. Therefore, these are higher than D_{TEM}, which considers the particles in a dried state.

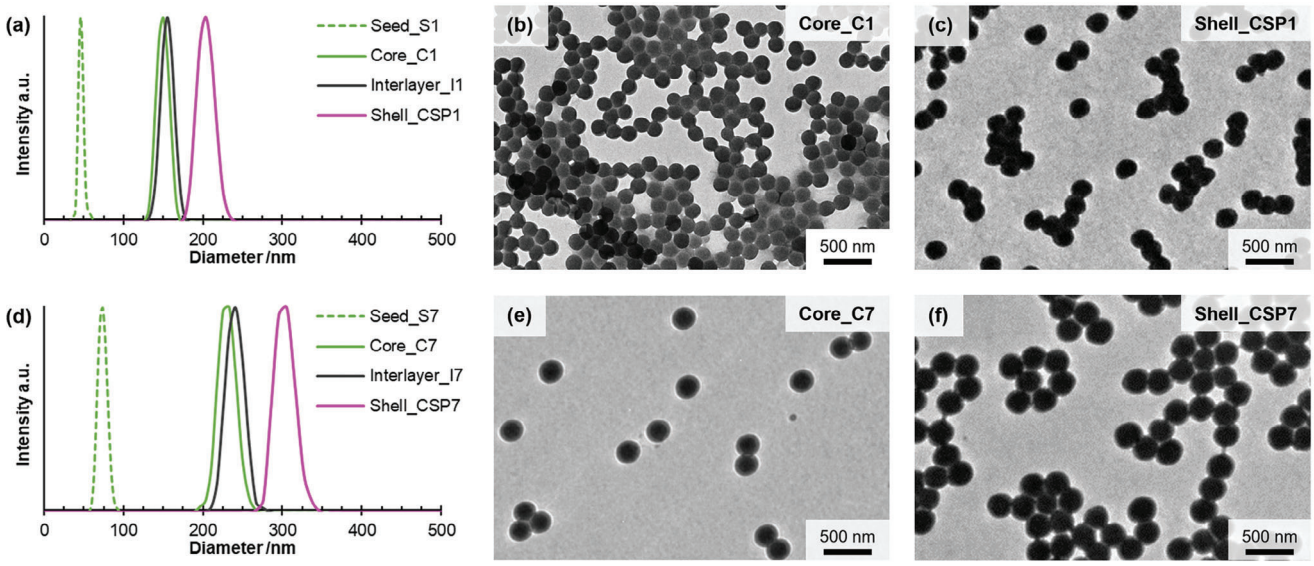

Figure 2. DLS measurements and TEM images of(a–c) batch CSP1 (smallest particle diameter) and d–f) batch CSP7 (largest particle diameter). Analogous measurements for the other batches CSP2-6 are depicted in the Supporting Information (Figure S1, Supporting Information).

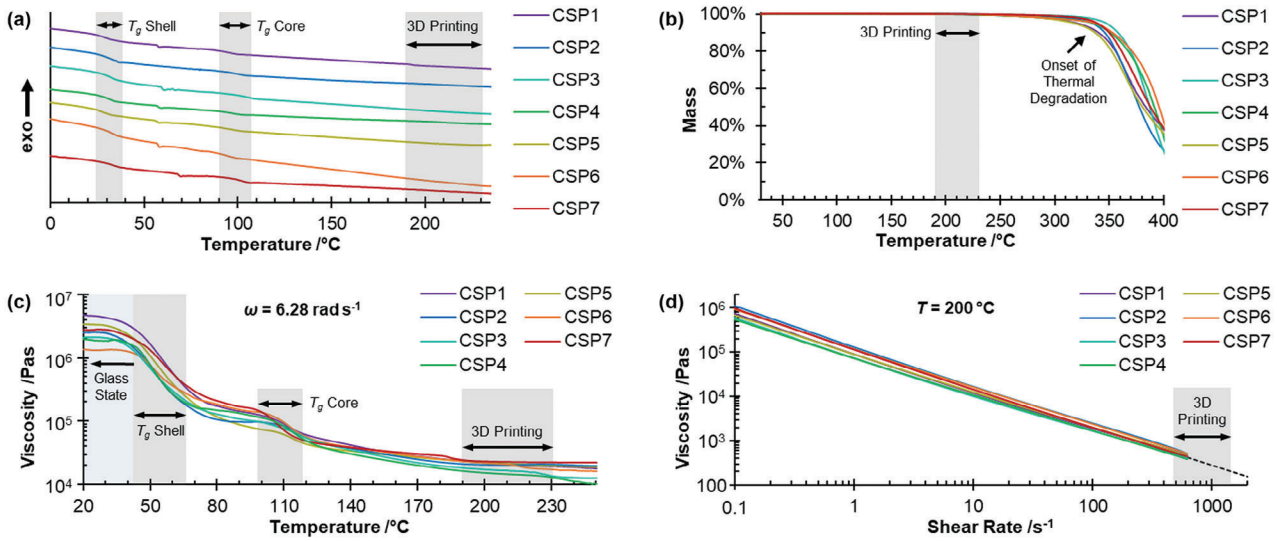

Figure 3. Thermal and rheological analysis of the filaments. a) DSC measurements. b) TGA data. c) Temperature-dependent viscosities at an angular frequency of 6.28 rad s^{-1}. d) Frequency-dependent viscosities at the printing temperature of 200 °C, wherein the dotted black line indicates an extrapolation according to the Ostwald-deWaele power law as calculated in the Supporting Information (Table S1, Supporting Information).

Prior to the shell synthesis, an interlayer consisting of poly(methyl methacrylate-*co*-allyl methacrylate) (P(MMA-*co*-ALMA)) was introduced. While the acrylic moiety of ALMA was copolymerized with MMA during interlayer synthesis, the less reactive allylic moiety enabled covalent anchoring of the shell polymer in a subsequent grafting-through reaction. Such grafting was necessary to ensure processing stability: The covalent linkages prevented detachments of shell polymer chains and phase separation during filament extrusion and 3D printing.[10a,d] A certain amount of ALMA was necessary to graft all shell polymer chains quantitatively, but the content had to be limited to an optimized proportion of 5 wt%. At higher contents, unconsumed grafting anchors could have led to a thermally induced cross-linking between separate particles during processing. This would have resulted in a loss of malleability and embrittlement, thus impeding processibility.[5c] The successful implementation of the interlayer was confirmed by DLS data (Figure 2; Figure S1, Supporting Information).

In the final synthesis step, the particle shell consisting of poly(methyl methacrylate-*co*-ethyl acrylate) (P(MMA-*co*-EA)) was introduced. The shell-forming monomer emulsion used a mixture of 50 wt% MMA and 50 wt% EA. While literature-known CSP usually feature an elastomeric shell,[5c,10a,d] the incorporation of MMA in this work led to a shift in glass transition above room temperature (**Figure 3**). The thus obtained thermoplastic material properties were an essential prerequisite for filament-based 3D printing, as the shell polymer chains of all particles formed a continuous, fluid phase at elevated processing temperatures.

During synthesis, a precise adjustment of the core-to-shell ratio was necessary. On the one hand, core proportions below 40% would have led to a loss of structural color quality. The increased space between individual core particles impedes self-assembly into a colloidal crystalline structure. On the other hand, core proportions substantially above 45% would have been unfavorable for processability. Without enough shell polymer, the highly cross-linked cores possess the rheological properties of a rigid thermoset and are neither malleable nor show considerable plastic flow at any temperature.[5c] According to TEM data in Table 1, a core proportion of 43 ± 2 vol% was achieved, thus confirming that high control over the polymerization was exercised and that the desired core-to-shell ratio was achieved. Given the fixed core- and shell-proportions, larger core particles inevitably led to larger CSP. Hence, different particle sizes were only achievable by varying the core particle size, as described above. The continuous addition of monomer in starved-feed mode ensured that particles with uniform size were obtained, no secondary nucleation occurred, and the desired core–shell architecture was achieved. The low standard deviations of <5% for D_{TEM} and polydispersity indices (PDI) of ≤0.05 for D_{DLS} confirmed the excellent monodispersity of all seven batches, which was mandatory to enable the arrangement into a highly ordered photonic crystal in the following processing steps.

2.2. Filament Extrusion and 3D Printing

After synthesis, the CSP were freeze–dried, and a fluffy white powder was obtained. No structural color could be observed, as the particles were not yet organized in a colloidal ordered structure. Before filament extrusion, the CSP were homogenously mixed with small amounts of three different additives. Carbon black was added at a weight proportion of 0.03 wt%, which is known to improve color saturation for CSP-based opals[20] and other structural color materials.[21] The primary antioxidant pentaerythritol-tetrakis(3-[3,5-di-*tert*-butyl-4-hydroxyphenyl]propionate), commonly known as Antioxidant 1010, was added at a weight proportion of 1.5 wt%. In a previous study, it has been shown that this type of antioxidant enhances thermal stability when used in combination with the above-described optimized particle architecture.[5c] Finally, 2.0 wt% of the plasticizer diisononylphthalate (DINP) was added,

which reduced brittleness and thus enabled faster filament spooling.

After homogenously incorporating the additives, filaments of each batch CSP1-7 were extruded, and their thermo-rheological properties were analyzed. The different batches yielded almost identical results, thus confirming the excellent reproducibility of the applied synthesis and processing protocols. Differential scanning calorimetry (DSC) revealed the glass transitions of the P(EA-*co*-MMA) shell at 32 ± 1 °C and the cross-linked PS cores at 99 ± 4 °C (Figure 3a). The presence of two glass transitions further confirmed that a well-defined core–shell architecture was obtained. It was of particular importance that the glass transition of the shell was above room temperature to equip the filaments with thermoplastic properties. Literature-known CSPs usually feature shell polymers with glass transitions below room temperature, rendering them unsuitable for FDM printing. With such an elastomeric shell, the developed extrusion forces are too low, owing to the low stiffness and poor buckling resistance. Moreover, the filament extruder gears can penetrate the soft surface, digging into the material and thus eroding or scraping off the filament structure instead of pushing it downward.

The DSC thermograms were inconspicuous at 3D printing temperatures of 190 to 230 °C, thus indicating thermal stability in this range. To further investigate the filaments' temperature stability, thermogravimetric analyses (TGA) were performed (Figure 3b). For all seven batches, the onset of thermal degradation was around or above 300 °C, substantially higher than the relevant temperatures for FDM.

Temperature-dependent viscosities of all batches are depicted in Figure 3c. While the filaments were in a glassy state at room temperature, large viscosity drops over a decade were observed between 40–70 °C. This can be attributed to the glass transition of the thermoplastic shell polymer at 56 ± 1 °C. The glass transition was shifted to higher temperatures than the previously discussed DSC measurements. Besides differences in the measurement principles and heating rates, the dependence of the glass transition on the measurement frequency of the oscillatory shearing can sufficiently explain this deviation, as the glass transition temperature was found to decrease with decreasing frequency (Figure S2, Supporting Information). Above the glass transition of the shell, viscosities asymptotically reduced up to 250 °C, following an Arrhenius-type progression. The minor viscosity drops at 100–120 °C relate to the glass transition of the core particles at 113 ± 3 °C. Due to the cross-linked nature of the cores, their glass transition hardly influenced the overall course of the temperature-dependent viscosity. The rheological properties of the core particles resembled a non-deformable thermoset rather than a malleable thermoplastic polymer. This was favorable, as they had to retain their round shape during processing for successful self-assembly. Finlayson et al. and our group have previously investigated the temperature-dependent rheological properties of CSP with an elastomeric shell, revealing that the shell material mainly determines the thermo–rheological properties.[5b,c,10a,22] In analogy to these findings, the filament's rheology was also found to be predominantly governed by the thermoplastic nature of the shell quasi-matrix.

The suitability of the filaments for FDM was further enhanced by the strong shear-thinning behavior at the default printing temperature of 200 °C, as depicted in Figure 3d. Assuming the applicability of the Cox–Merz rule, the shear-dependent viscosity during printing $\eta(\dot{\gamma})$ was approximately equalized with the measured dynamic complex viscosity in dependence of the angular frequency $\eta^*(\omega)$. In contrast to the high zero-shear values, the viscosities of all batches dropped by roughly three orders of magnitude at 3D printing conditions. The shear rates during printing were calculated in Table S2 (Supporting Information). Owing to the vastly reduced viscosity at elevated temperatures and under shear forces, the filament could easily be extruded during 3D printing via FDM. Meanwhile, the downward-pushing filament strand was in a glassy state. The thermoplastic nature of the materials provided sufficient buckling resistance and created adequate force to push the heated, low-viscous material through the nozzle. Once printed, the material was cooled down below its glass transition and no longer exposed to shear forces. This led to a rapid increase in viscosity, thus providing dimensional accuracy and a stable foundation for the following layers.

In addition to the rheological analysis, we conducted mechanical tests of all filament batches at room temperature. An overview of the mechanical properties is compiled in Table S3 (Supporting Information). The Shore D Hardness was found to be 74 on average and thus in the typical range of hard thermoplastic polymers. Tensile tests (Figure S3, Supporting Information) revealed an average elongation at break of 4%, which is on a comparable level to commercially available filaments, such as ASA, ABS, or PLA. The determined tensile modulus of 793 MPa on average is considerably lower than commercial filaments, which often feature moduli above 1 GPa, thus indicating higher pliability. The average tensile strength of 21 MPa was found to be on the same order of magnitude as standard commercials, although on the lower end of the typical range.[1a,23] The lower stiffness and strength can be sufficiently explained by the absence of crystalline domains (on the molecular scale) and the comparably low glass transition of the herein-presented material. For most applications, however, mechanical strength and stiffness should be sufficient, especially when considering that print settings (layer height, orientation, infill, etc.) can be used to tune mechanical properties and that the material may be used for functional optics in combination with high-strength structural polymers. Overall, and analogous to the rheological properties, the mechanical properties turned out to be dominated by the thermoplastic shell polymer matrix.

Photographs of the filaments are illustrated in **Figure** 4a. Most objects in this work, including the owls in Figure 4b, were 3D printed with two perimeter outlines and 20% grid-type infill. The filaments printed best in a range of 190–230 °C with no buckling, steady flow, good layer adhesion, and sufficient shape stability after depletion. For better dimensional accuracy and performance in overhangs, a heated bed with a temperature of 70–80 °C and intense cooling were favorable. The use of a direct drive extruder enabled printing speeds up to 40 mm s^{-1}. The (vertical) resolution was determined by the layer height of 0.2 mm.

2.3. Structural Color

Figure 4a,b illustrate the vivid and opalescent structural colors of the filaments and thereof 3D printed owls, respectively. In accordance with Bragg's law, the different sizes of CSP1-7 led to different structural colors: The reflection gradually shifted to

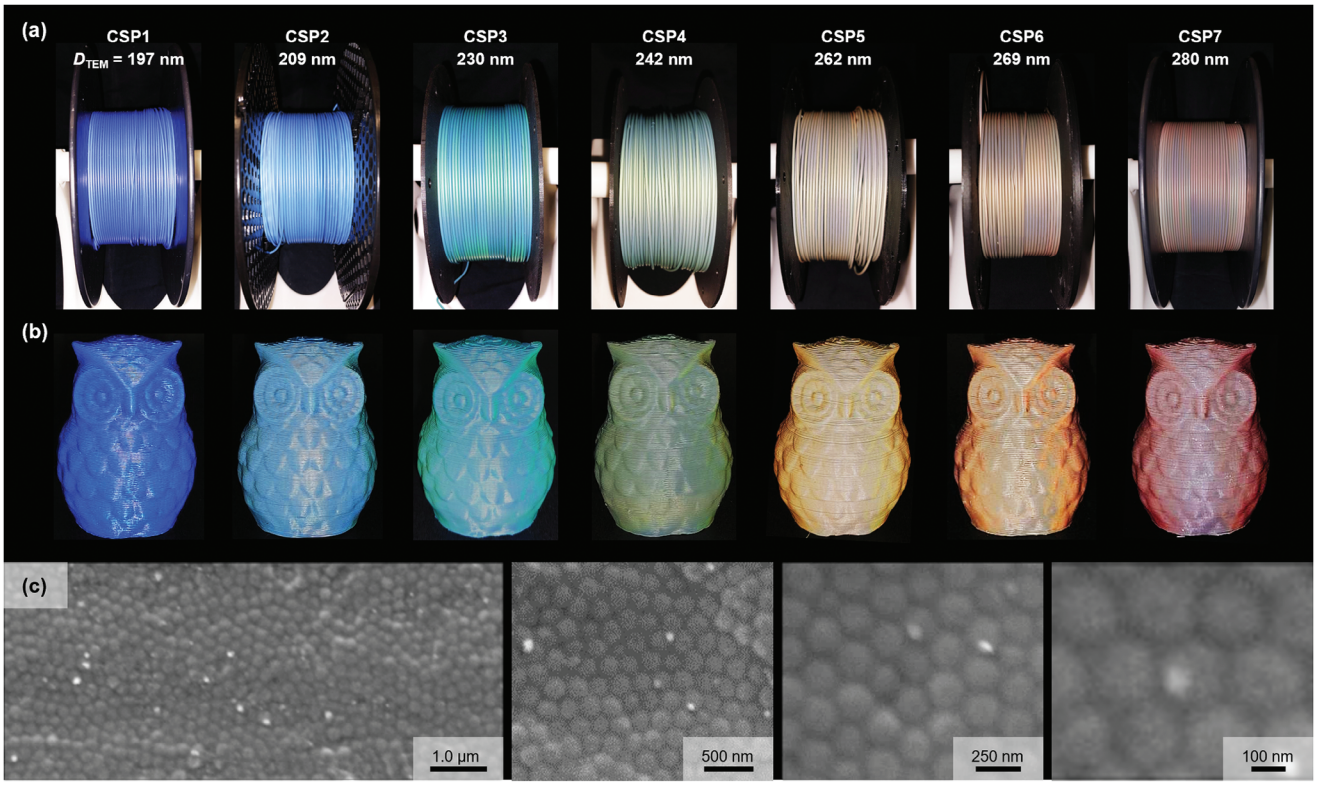

Figure 4. Photographs of a) filaments and b) 3D printed owls (height: 36 mm). The particle batches CSP1-7 differ exclusively in particle size *D*, causing different reflection colors. c) SEM images of printed surfaces of batch CSP5.

longer wavelengths with larger particle diameters. All colors in the visible range were covered, including violet, blue, turquoise, green, yellow, orange, and red. As described in the introduction, the cores of state-of-the-art CSP can self-assemble inside the continuous shell matrix when elevated temperatures and aligned shear forces are applied. Since filament extrusion and 3D printing fulfill these prerequisites, it appeared likely that the herein presented particles had analogously self-assembled into a photonic material, which led to the appearance of the observed structural color.

Scanning electron microscopy (SEM) experiments were conducted to investigate this thesis. Figure 4c shows the particle arrangement on printed surfaces as an example for batch CSP5. SEM images of all other batches are provided in the Supporting Information (Figure S4, Supporting Information). Microscopy revealed that short-range order had formed mostly in the typical hexagonal fashion of a closest-packed lattice structure. Large-view images appeared rather disordered and indicated imperfect long-range order.

The iridescence of printed objects was examined in **Figure 5** to investigate the ordered colloidal structure further. In general, iridescence results from the angle-dependency of structural color and requires long-range ordered photonic crystals.[3b,e,4f,21b] Photographs in the top row of Figure 5a were taken with a camera flashlight to mimic ideal vertical light incidence and reflection. Photos in the bottom row were taken with diffuse illumination, where light fell in from every direction between 0° and 90° (45° on average). The two different lighting conditions facilitated a color change of the printed objects. For example, the car made of CSP3 changed its appearance from turquoise to blue, and the crocodile made of CSP6 from orange to green. The reflection spectra in Figure 5b,c provided analytical proof of the visually perceived color shift. Every printed object showed a sharp reflection peak at vertical light incidence (90°), which shifted to shorter wavelengths when measured at an angle of 45°. According to the underlying structure–property relationship, this observation indicated that there had to be long-range order. In joint consideration with the SEM experiments, we assume that there is an imperfect, yet existing long-range order. Thus, 3D printed objects may be considered somewhere in between a photonic crystal and a photonic glass.

All peak reflection wavelengths were summarized in Figure 5d and sketched against the particle size. The dotted lines indicate the theoretically expected values, as calculated with Bragg's law in Table S4 (Supporting Information). The minimal deviations between measured and calculated values of <3% proved the excellent accordance with the underlying theory. Moreover, reflection colors were found to be independent of printing direction, orientation, speed, and temperature – at least in the relevant ranges for 3D printing (Figure S5, Supporting Information).

Overall, experimental results indicated that microstructure formation most likely proceeded comparably to what is known from films,[10e,17] fibers,[10c] and foils[10a,b] based on elastomeric CSP: Driven by aligned shear forces during processing at elevated temperatures, the rigid core particles self-assembled inside the viscous shell matrix. Due to the high monodispersity of the particles,

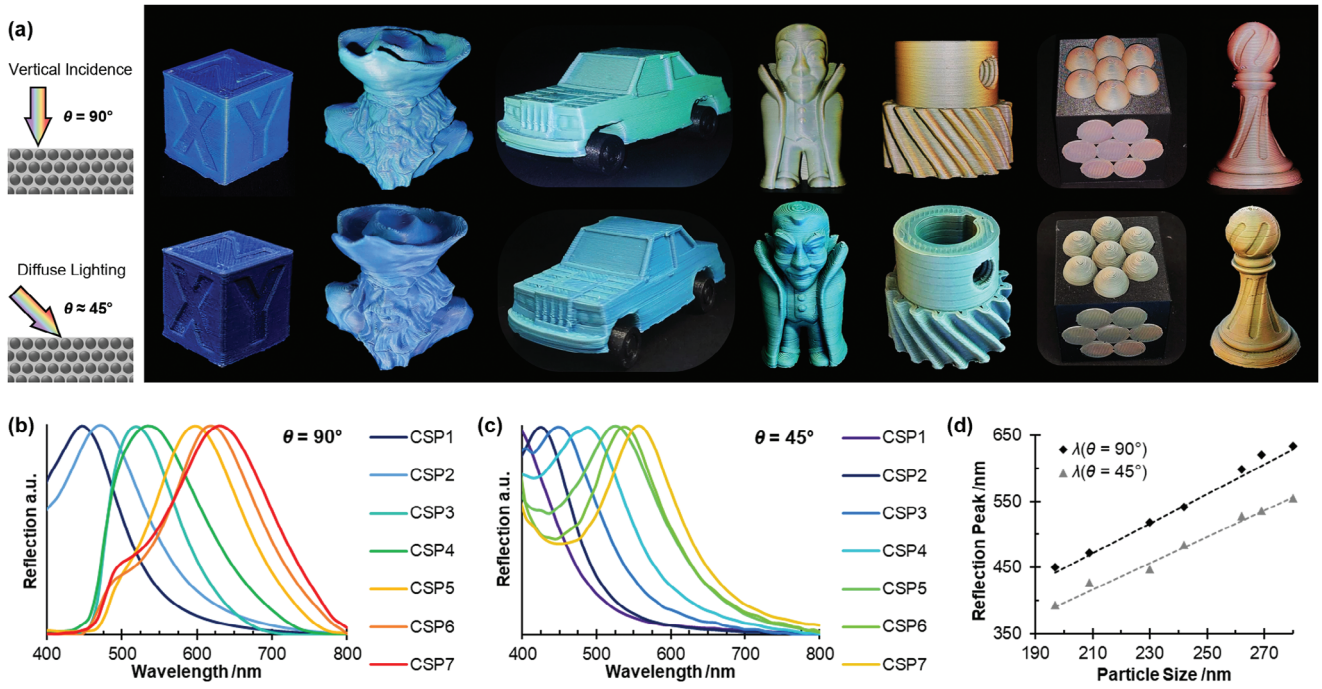

Figure 5. a) 3D printed objects made from CSP1-7 (from left to right, respectively) under different illumination conditions: calibration cube; pirate; car; vampire (digital STL model used under terms of the CC BY 4.0 license.[24] Copyright 2023, 3D-Printy); screw gear; hexagonal ordered particles; chess pawn (digital STL model used under terms of the CC BY 4.0 license.[25] Copyright 2023, Adam Tesar) Object sizes vary between 20 and 70 mm; detailed dimensions are provided in the Supporting Information (Figure S6, Supporting Information). b,c) Reflection spectra of flat printed surfaces at light incidences of 90° and 45°. d) Peaks of the reflection spectra; the dotted lines indicate the expected theoretical values.

good short-range order was achieved with a dominant hexagonal pattern. Moreover, (imperfect) long-range order was obtained, with the most closely packed direction of each domain favorably oriented parallel to the printed surface. The thus-formed colloidal-ordered structure is the underlying physical cause for the observed photonic properties and opalescent structural colors.

In comparison to commercial filaments, where coloration is achieved with artificial colorants, the herein-presented filaments are superior: Their structural color appears more vivid and with shimmering iridescence. Moreover, it can be tuned over the whole visible spectrum and does not require any additional dye or pigments, which are potentially toxic or environmentally harmful. These inherent advantages were combined with high resolution, dimensional accuracy, geometrical complexity, and surface quality. Given that the filaments were printed on the commercial desktop printer Prusa I3 MK3S+, it was thus demonstrated that the possibilities of printable objects are comparable to state-of-the-art filaments. Therefore, potential uses can be found in all the ever-growing application fields of FDM 3D printing. These include but are not limited to construction, rapid prototyping, automotive, aerospace, medical devices, decor, toys, and education.

Another exceptional property sets the material apart from state-of-the-art filaments: The transmission color when looking through the material against a light source. By Bragg's law, wavelengths that do not interfere constructively with the periodic structure pass through the material unhindered. **Figure 6a** shows photographs and spectra of a 3D-printed gecko of CSP5 in angle-dependent reflection and transmission. Upon increase of the viewing angle from 30° to 90°, the wavelength shifted by ≈100 nm, concomitant with a color change from green to yellow–orange. In transmission, a further bathochromic shift to red was observed. A similar analysis for CSP4 is provided in Figure 6b. A printed surface of CSP4 makes up the house's windows, while the black parts were printed with a commercial PLA filament without structural color. Only by alterations of illumination, the color did change from blue (30°) over green (90°) to orange (transmission), hence covering almost the entire visible spectrum with one single batch. Angle-dependent reflection spectra and transmission spectra for all other batches are provided in Figure S7 (Supporting Information). Surprisingly, all angle-dependent spectra showed increasing reflection intensities at wavelengths ≤450 nm as soon as the angle of light incidence was flatter than vertical incidence (90°). An extensive discussion of this phenomenon is provided in the context of Figure S8 (Supporting Information).

In principle, the 2D objects in Figure 6a,b could have also been produced from films or foils using established processing methods. The approach herein presented, however, offered the advantages of quick customizability and adaptability with high accuracy and integrity. Moreover, since FDM is a rapid and automated one-step fabrication process, it does not require post-processing or a mask, mold, form, or the like. The unique ability of 3D printing for precise and convenient control over the part thickness by variations of the number of layers or the layer thickness/height ensured the highest level of accuracy in our results. The last aspect was also utilized in Figure 6c to create lithophanes. In reflection, the top and bottom surface of the print exhibited a blue

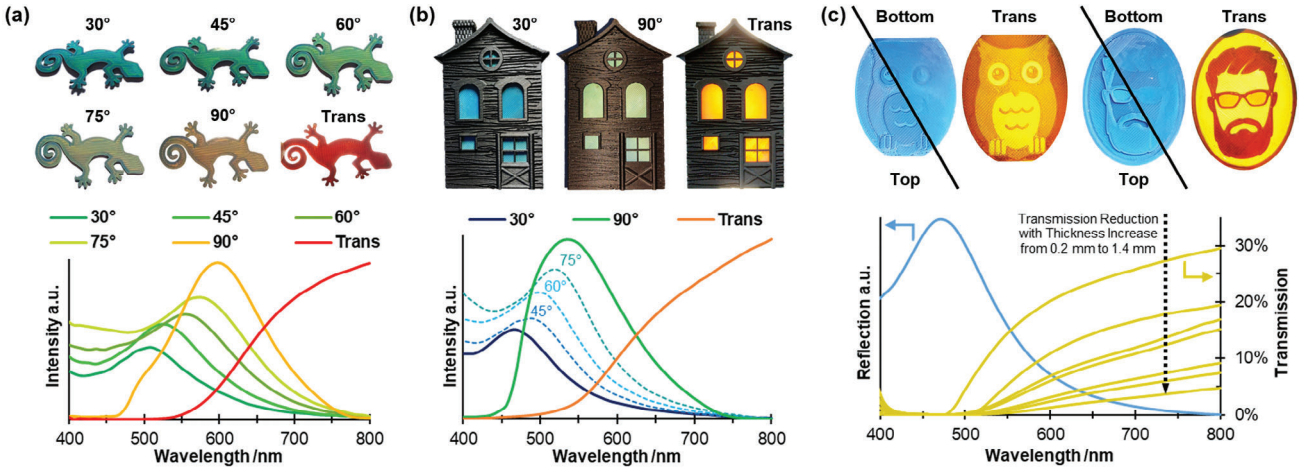

Figure 6. a) Photographs of a 3D printed gecko made of CSP5 under different illumination conditions and the corresponding angle-dependent reflection spectra and transmission spectrum. Digital STL model used under terms of the CC BY 4.0 license.[26] Copyright 2023, Gordyt47. b) A house made of black PLA with 3D printed windows of CSP4 and the corresponding angle-dependent reflection spectra and transmission spectrum. c) Photographs and spectra of two lithophanes, showing an owl and a bearded person. The diagram shows the corresponding reflection spectrum at 90° and transmission spectra depending on the part thickness, that is, the number of layers with a height of 0.2 mm each. Detailed dimensions of all objects (Figure S6, Supporting Information) and angle-dependent reflection and transmission spectra (Figure S7, Supporting Information) of all other batches are provided in the Supporting Information.

structural color. When looked through against a light source, the complimentary color became visible, appearing as different shades of yellow. As shown in the transmission spectra, intensity decreased with each additional layer. Such an effortless local variation of transmission intensity is hardly possible with state-of-the-art processing techniques.

In addition to the above-described usages, the unique iridescence and transmission properties of the 3D prints further broaden application potentials. Due to the inherent properties of structural colors, the intensity and position of the reflected or transmitted wavelengths are not subject to fluctuations, and the dynamic color change occurs instantly with unlimited reversibility. These features qualify the material for advanced optical filters, display applications, or tamper-proof security features.

The possibility of recycling further boosts the inherently high sustainability of the materials. Failed or superfluous prints, printing scraps (support structures, brims, skirts, etc.), and filament residues could be re-extruded alone or with "fresh" polymer. These recycled filaments could be printed without alterations. To prove recyclability, three calibration cubes were produced and analyzed (Figure S9, Supporting Information). The first one was printed with filament composed of the as-synthesized CSP4 and the obligatory additives (cycle 1). Afterward, 3D-printed objects and leftovers from cycle 1 were re-extruded and re-spooled. The thus obtained recycled filament was used to print the second cube (cycle 2). This procedure was repeated with material from cycle 2. Thereby, a twice-cyled filament was prepared, which was used to print the third cube (cycle 3). The cubes were not only visually indistinguishable from one another but also showed almost identical thermo–rheological and optical properties. While recyclability over a few cycles was thus proven, it must be noted that after a certain number of cycles, the antioxidant will be consumed. This, however, does not impede recyclability since new antioxidant can be conveniently added during the re-extrusion of the filament.

3. Conclusion

We presented a convenient fabrication method for a 3D printing filament with tunable and iridescent structural color. Inspired by nature, core–shell particles with tailored thermo–rheological properties were synthesized and processed. Particle size was demonstrated to be tunable during core synthesis. Since particle size directly correlates with the reflected wavelength, the opalescent filaments are available in all colors on the rainbow. Our system outperforms previous 3D printing approaches for structural color materials in terms of printing speed, resolution, level of detail, object complexity, compatibility with commercial desktop printers, and/or color quality. An overall high printing quality, comparable to state-of-the-art commercial filaments, was successfully combined with the inherent sustainability and advantages of structural colors. Depending on light incident conditions or viewing angle, the same print can exhibit several different colors, for example, from blue over green to orange. The potential for widespread use is facilitated by the simplicity and scalability of our approach. Only standard monomers and additives were processed, which are also used for commercial filaments. Moreover, emulsion polymerization is suitable for large-scale manufacturing and represents a widespread method for industrial polymer synthesis. We envision these filaments as alternatives and supplements in almost all typical 3D printing applications, such as tailored spare parts, helpful gadgets, and tools, educational models, tabletop miniatures, or toys. Other relevant markets are personalized merchandising items, apparel, and household décor, such as interior and exterior furnishings or seasonal decorations. Moreover, the opalescent appearance facilitates applications for anti-counterfeiting, advanced displays, or camouflage materials. In perspective, stimuli-responsive behavior, known from state-of-the-art CSP, could also be implemented. Responsivities to temperature, pH, humidity, electricity, and other stimuli will further

broaden application potentials in fields such as smart sensing, customized optical devices, or 4D printing.

4. Experimental Section

Materials: Styrene (99%) was obtained from Fisher Scientific. BDDA (90%), MMA (99%), EA (99.5%), potassium hydroxide flakes (KOH, reagent grade), sodium disulfite (NaDS, analysis grade), sodium persulfate (NaPS, ≥98%), and sodium dodecyl sulfate (SDS, ≥98.5%) were obtained from Sigma-Aldrich. ALMA (98%) and DINP (technical grade) were obtained from TCI. Disodium isododecyl phenyl ether sulfonate (DIPES) was purchased from Ezkem. Carbon Black (Channel Type Black 4) was obtained from Evonik. Antioxidant1010 was obtained from Nordmann-Rassmann under the tradename Norantox1010.

Instrumentation for Polymer Analysis: DLS measurements were carried out on a Zetasizer ZS 90 by Malvern Instruments at an angle of 90° with a fivefold determination of 15 runs and automated data acquisition in 300 size classes. A cumulants analysis gave an intensity mean value ("z-average") for the hydrodynamic diameter D_{DLS} with the PDI as the width parameter. The polymer dispersion was drop-casted on a carbon-coated copper grid for TEM experiments and dried for 24 h in an ambient laboratory atmosphere. TEM experiments were conducted using a JEOL JEM-2100 electron microscope at a nominal acceleration voltage of 200 kV with a Gatan Orius SC100 CCD camera in bright field mode. To determine average particle diameters D_{TEM}, 25 particles per image were analyzed using ImageJ software. SEM experiments were carried out on a Zeiss Gemini500 Sigma VP device using the software SmartSEM Version 6.07, with accelerating voltages between 2 and 4 kV. DSC and TGA measurements were carried out using a Netzsch 214 F1 Polyma and a Netzsch TG 209 F1 Libra, respectively, both with a heating rate of 10 K min^{-1} under a synthetic air atmosphere. Temperature-dependent (heating rate 3 K min^{-1}; frequency 1 Hz; angular frequency $\omega = 6.28$ rad s^{-1}) and frequency-dependent (isothermal temperature $T = 200$ °C) rheological properties were determined with an Anton Paar MCR 302e oscillatory rheometer, using a 25 mm plate–plate geometry in an ambient laboratory atmosphere. Glass transitions were defined as the maximum of the loss factor. Tensile tests were performed using a Zwick–Roell universal testing machine with a testing speed of 1.0 mm s^{-1} and the software testXpert II. Shore D Hardness was determined using a Sauter HBD 100-0 Durometer. Reflection spectra were recorded with an Ocean Optics fiber FLAME spectrometer USB2000, combined with an Ocean Optics deuterium–tungsten halogen lamp DT mini-2. The reflection intensities of each batch were calibrated with a white reflectance standard by Thorlabs (PMR10P1) and normalized concerning the reflection intensity at normal light incidence ($\theta = 90°$) of the respective printed surface. Transmission spectra were calibrated relative to the unaltered light source. When directly compared to reflection spectra, transmission intensities were normalized to arbitrary units for better visual comparability.

Particle Synthesis: Before emulsion polymerization, radical inhibitors were removed from all monomers by passing them through a basic alumina column (50–200 µm, Acros Organics). The P(S-*co*-BDDA) core synthesis of C1 was carried out as follows: A double-wall reactor under nitrogen atmosphere at 75 °C was filled with the seed-forming monomer emulsion of 0.539 g SDS, 525 g deionized water, 6.75 g styrene, 0.750 g BDDA. While stirring at 200–225 rpm, the polymerization was initiated with 0.135 g NaDS and 0.971 g NaPS. After a reaction time of 10 min, the core-forming monomer emulsion was added in starved-feed mode, using a rotary piston pump at a flow rate of 1.4 mL min^{-1}. This monomer emulsion contained 0.195 g DIPES, 0.204 g SDS, 0.355 g KOH, 62.1 g styrene, 79.8 g deionized water, and 6.21 g BDDA. Afterward, the emulsion was stirred for another 60 min at a constant temperature, drained from the reactor, and diluted to a solid content of 8.0 wt%. To increase particle size for the other batches C2-7, the SDS proportion in the seed stage was reduced, and the amount of added monomer emulsion in starved-feed mode was increased, as described in the literature.[20c,27] For the typical interlayer- and shell synthesis, 549 g of the respective diluted core dispersion were filled in a double-wall reactor under a nitrogen atmosphere at 75 °C. While stirring at 200 rpm, the emulsion polymerization was initiated with 0.117 g NaDS and 0.681 g NaPS. After a reaction time of 15 min, the interlayer-forming monomer emulsion was continuously added with a rotary piston pump at a flow rate of 2.0 mL min^{-1}. This monomer emulsion consisted of 0.133 g DIPES, 0.367 g ALMA, 6.97 g MMA, 0.067 g SDS, and 29.6 g deionized water. After 15 min, the polymerization was reinitiated with 0.100 g NaPS and stirred for another 10 min. Subsequently, the shell-forming monomer emulsion was added with a rotary piston pump at a flow rate of 2.0 mL min^{-1}. This monomer emulsion consisted of 0.361 g SDS, 45.9 g EA, 45.9 g MMA, 0.292 g DIPES, 120 g deionized water, and 0.509 g KOH. Finally, the reaction mixture was kept at a constant temperature and stirred for an additional 60 min. This recipe was used for all interlayer- and shell syntheses with minor alterations: The overall batch size was decreased from 800 to 400 g for CSP1 and 707 g for CSP5; the addition flow rate was decreased accordingly to 1.0 and 1.8 mL min^{-1}, respectively. Moreover, the ratio of initially added core dispersion (containing 8 wt% of already polymerized core particles) to interlayer- and shell-forming monomer emulsion was varied by ±5% between batches. Thereby, slight yield fluctuations during interlayer- and shell-syntheses were compensated to achieve the targeted core-to-shell ratio in the final CSP.

Processing: After synthesis, each batch was freeze–dried and mixed with 0.03 wt% carbon black, 1.5 wt% Antioxidant1010, and 2.0 wt% DINP. The homogenized mixtures were extruded into filament strands using a Thermo Scientific HAAKE MiniLab 3 Micro-Compounder at 140 °C and 50 rpm, equipped with a round 1.75 mm die. The obtained filaments were printed on a Saarpricom Delta UpSD printer (equipped with a filament extrusion head) and a Prusa MK3S+; both equipped with 0.4 or 0.6 mm brass nozzles. Slicing was performed with Simplify3D and PrusaSlicer. 3D printing models were created with Autodesk Inventor and Blender or used under the indicated Creative Commons Licenses.

Supporting Information

Supporting Information is available from the Wiley Online Library or from the author.

Acknowledgements

The authors thank Sebastian Pusse and Regina Leiner for the TEM experiments. The authors thank the group of Prof. Volker Presser (Leibniz Institute for New Materials), Till Rittner, and Sebastian Heinz for SEM experiments. The authors acknowledge the support of Rafael Valentin and Sascha Verwaayen during particle syntheses. The authors declare the following financial interests and personal relationships that may be considered potential competing interests: Lukas Siegwardt has patent #EP 23210135.2 pending at Saarland University, and Markus Gallei has patent #EP 23210135.2 pending at Saarland University.

Open access funding enabled and organized by Projekt DEAL.

Conflict of Interest

The authors declare no conflict of interest.

Data Availability Statement

The data that support the findings of this study are available from the corresponding author upon reasonable request.

Keywords

additive manufacturing, biomimetics, colloids, emulsion polymerization, fused filament fabrication, photonic materials, self-assembly

Received: June 27, 2024
Revised: September 11, 2024
Published online: October 17, 2024

[1] a) K. Rajan, M. Samykano, K. Kadirgama, W. S. W. Harun, M. M. Rahman, *Int. J. Adv. Manuf. Technol.* **2022**, *120*, 1531; b) M. Askari, D. A. Hutchins, P. J. Thomas, L. Astolfi, R. L. Watson, M. Abdi, M. Ricci, S. Laureti, L. Nie, S. Freear, R. Wildman, C. Tuck, M. Clarke, E. Woods, A. T. Clare, *Addit. Manuf.* **2020**, *36*, 101562; c) M. Falahati, P. Ahmadvand, S. Safaee, Y. C. Chang, Z. Lyu, R. Chen, L. Li, Y. Lin, *Mater. Today.* **2020**, *40*, 215; d) M. Su, Y. Song, *Chem. Rev.* **2021**, *122*, 5144; e) S. C. Ligon, R. Liska, J. Stampfl, M. Gurr, R. Mülhaupt, *Chem. Rev.* **2017**, *117*, 10212.

[2] a) P. V. Braun, *Nature.* **2011**, *472*, 423; b) M. Li, Q. Lyu, B. Peng, X. Chen, L. Zhang, J. Zhu, *Adv. Mater.* **2022**; c) R. Xiong, J. Luan, S. Kang, C. Ye, S. Singamaneni, V. V. Tsukruk, *Chem. Soc. Rev.* **2020**, *49*, 983; d) G. Isapour, M. Lattuada, *Adv. Mater.* **2018**, *30*, 1707069; e) J. V. Sanders, *Nature.* **1964**, *204*, 1151; f) J. Teyssier, S. V. Saenko, D. van der Marel, M. C. Milinkovitch, *Nat. Commun.* **2015**, *6*, 6368; g) M. Vatankhah-Varnosfaderani, A. N. Keith, Y. Cong, H. Liang, M. Rosenthal, M. Sztucki, C. Clair, S. Magonov, D. A. Ivanov, A. V. Dobrynin, S. S. Sheiko, *Science.* **2018**, *359*, 1509.

[3] a) M. Li, B. Peng, Q. Lyu, X. Chen, Z. Hu, X. Zhang, B. Xiong, L. Zhang, J. Zhu, *Nat. Commun.* **2024**, *15*, 1874; b) L. Schertel, S. Magkiriadou, P. Yazhgur, A. Demirörs, *Chimia.* **2022**, *76*, 833; c) Z. Cai, Z. Li, S. Ravaine, M. He, Y. Song, Y. Yin, H. Zheng, J. Teng, A. Zhang, *Chem. Soc. Rev.* **2021**, *50*, 5898; d) L. Shang, W. Zhang, K. Xu, Y. Zhao, *Mater. Horiz.* **2019**, *6*, 945; e) N. Vogel, M. Retsch, C. A. Fustin, A. Del Campo, U. Jonas, *Chem. Rev.* **2015**, *115*, 6265; f) B. E. Droguet, H. L. Liang, B. Frka-Petesic, R. M. Parker, M. F. L. De Volder, J. J. Baumberg, S. Vignolini, *Nat. Mater.* **2022**, *21*, 352; g) J. H. Moon, S. Yang, *Chem. Rev.* **2010**, *110*, 547.

[4] a) G. Li, M. Leng, S. Wang, Y. Ke, W. Luo, H. Ma, J. Guan, Y. Long, *Mater. Today.* **2023**, *69*, 133; b) H. Gao, J. An, C. K. Chua, D. Bourell, C. N. Kuo, D. T. H. Tan, *Mater. Today.* **2023**, *69*, 107; c) C. f. Zhao, J. Wang, Z. q. Zhang, C. Chi, *Adv. Mater. Technol.* **2022**, *8*, 2200257; d) R. T. Shafranek, S. C. Millik, P. T. Smith, C. U. Lee, A. J. Boydston, A. Nelson, *Prog. Polym. Sci.* **2019**, *93*, 36; e) J. B. Kim, H. Y. Lee, C. Chae, S. Y. Lee, S. H. Kim, *Adv. Mater.* **2024**, *36*, 2307917; f) Y. Kang, J. Zhao, Y. Zeng, X. Du, Z. Gu, *Small.* **2024**, 2403525.

[5] a) B. B. Patel, D. J. Walsh, D. H. Kim, J. Kwok, B. Lee, D. Guironnet, Y. Diao, *Sci. Adv.* **2020**, *6*, eaaz7202; b) L. Siegwardt, M. Gallei, *Adv. Funct. Mater.* **2023**, *33*, 2213099; c) L. Siegwardt, M. Gallei, *J. Chem. Eng.* **2024**, *480*, 148168; d) A. T. L. Tan, S. Nagelberg, E. Chang-Davidson, J. Tan, J. K. W. Yang, M. Kolle, A. J. Hart, *Small.* **2020**, *16*, 1905519; e) P. Yazhgur, N. Muller, F. Scheffold, *ACS Photonics.* **2022**, *9*, 2809.

[6] a) J. S. Llorens, L. Barbera, A. F. Demirörs, A. R. Studart, *Adv. Mater.* **2023**, *35*, 2302868; b) A. T. Tan, J. Beroz, M. Kolle, A. J. Hart, *Adv. Mater.* **2018**, *30*, 1803620; c) H. K. Raut, H. Wang, Q. Ruan, H. Wang, J. G. Fernandez, J. K. W. Yang, *Nano Lett.* **2021**, *21*, 8602; d) H. Liu, H. Wang, H. Wang, J. Deng, Q. Ruan, W. Zhang, O. A. M. Abdelraouf, N. S. S. Ang, Z. Dong, J. K. W. Yang, H. Liu, *ACS Nano.* **2022**, *16*, 8244.

[7] a) F. K. Aldawood, *Actuators.* **2023**, *12*, 101; b) Z. Jiang, B. Diggle, M. L. Tan, J. Viktorova, C. W. Bennett, L. A. Connal, *Adv. Sci.* **2020**, *7*, 2001379.

[8] B. M. Boyle, T. A. French, R. M. Pearson, B. G. McCarthy, G. M. Miyake, *ACS Nano.* **2017**, *11*, 3052.

[9] a) X. Xu, S. A. Asher, *J. Am. Chem. Soc.* **2004**, *126*, 7940; b) T. Winter, M. Bitsch, F. Müller, S. Voskian, T. A. Hatton, K. Jacobs, V. Presser, M. Gallei, *ACS Appl. Polym. Mater.* **2021**, *3*, 4651; c) T. Winter, X. Su, T. A. Hatton, M. Gallei, *Macromol. Rapid. Commun.* **2018**, *39*, 1800428.

[10] a) C. E. Finlayson, J. J. Baumberg, *Materials.* **2017**, *10*, 688; b) Q. Zhao, C. E. Finlayson, D. R. Snoswell, A. Haines, C. G. Schäfer, P. Spahn, G. P. Hellmann, A. V. Petukhov, L. Herrmann, P. Burdet, P. A. Midgley, S. Butler, M. Mackley, Q. Guo, J. J. Baumberg, *Nat. Commun.* **2016**, *7*, 11661; c) C. E. Finlayson, C. Goddard, E. Papachristodoulou, D. R. Snoswell, A. Kontogeorgos, P. Spahn, G. P. Hellmann, O. Hess, J. J. Baumberg, *Opt. Express.* **2011**, *19*, 3144; d) M. Gallei, *Macromol. Rapid. Commun.* **2018**, *39*, 1700648; e) O. L. J. Pursiainen, J. J. Baumberg, H. Winkler, B. Viel, P. Spahn, T. Ruhl, *Adv. Mater.* **2008**, *20*, 1484.

[11] a) G. von Freymann, V. Kitaev, B. V. Lotsch, G. A. Ozin, *Chem. Soc. Rev.* **2013**, *42*, 2528; b) C. E. Finlayson, J. J. Baumberg, *Polym. Int.* **2013**, *62*, 1403; c) J. F. Galisteo-Lopez, M. Ibisate, R. Sapienza, L. S. Froufe-Perez, A. Blanco, C. Lopez, *Adv. Mater.* **2011**, *23*, 30; d) L. Gonzalez-Urbina, K. Baert, B. Kolaric, J. Perez-Moreno, K. Clays, *Chem. Rev.* **2012**, *112*, 2268.

[12] L. Siegwardt, V. Glossner, A. Boehm, M. Schneider, M. Gallei, *ACS Appl. Mater. Interfaces.* **2024**, *16*, 10722.

[13] D. Scheid, C. Lederle, S. Vowinkel, C. G. Schäfer, B. Stühn, M. Gallei, *J. Mater. Chem. C.* **2014**, *2*, 2583.

[14] a) C. G. Schäfer, C. Lederle, K. Zentel, B. Stuhn, M. Gallei, *Macromol. Rapid. Commun.* **2014**, *35*, 1852; b) C. G. Schäfer, M. Biesalski, G. P. Hellmann, M. Rehahn, M. Gallei, *J. Nanophotonics.* **2013**, *7*, 070599.

[15] a) C. G. Schäfer, M. Gallei, J. T. Zahn, J. Engelhardt, G. P. Hellmann, M. Rehahn, *Chem. Mater.* **2013**, *25*, 2309; b) M. Bitsch, A. K. Boehm, A. Grandjean, G. Jung, M. Gallei, *Molecules.* **2021**, *26*, 7350.

[16] a) W. Wang, Y. Zhou, L. Yang, X. Yang, Y. Yao, Y. Meng, B. Tang, *Adv. Funct. Mater.* **2022**, *32*, 2204744; b) W. Hong, Z. Yuan, X. Chen, *Small.* **2020**, *16*, 1907626; c) Q. Lyu, M. Li, L. Zhang, J. Zhu, *Macromol. Rapid Commun.* **2022**, *43*, 2100867; d) C. Fenzl, T. Hirsch, O. S. Wolfbeis, *Angew. Chem., Int. Ed.* **2014**, *53*, 3318.

[17] T. Ruhl, P. Spahn, G. P. Hellmann, *Polymer.* **2003**, *44*, 7625.

[18] CreativeTools, #3DBenchy, https://www.3DBenchy.com (accessed: May 2024).

[19] H. S. Wong, M. Mackley, S. Butler, J. Baumberg, D. Snoswell, C. Finlayson, Q. Zhao, *J. Rheol.* **2014**, *58*, 397.

[20] a) O. L. J. Pursiainen, J. J. Baumberg, H. Winkler, B. Viel, P. Spahn, T. Ruhl, *Opt. Express.* **2007**, *15*, 9553; b) O. L. J. Pursiainen, J. J. Baumberg, K. Ryan, J. Bauer, H. Winkler, B. Viel, T. Ruhl, *Appl. Phys. Lett.* **2005**, *87*, 101902; c) T. Ruhl, *Dissertation*, TU Darmstadt, Darmstadt **2003**.

[21] a) J. D. Forster, H. Noh, S. F. Liew, V. Saranathan, C. F. Schreck, L. Yang, J. G. Park, R. O. Prum, S. G. Mochrie, C. S. O'Hern, H. Cao, E. R. Dufresne, *Adv. Mater.* **2010**, *22*, 2939; b) L. Schertel, L. Siedentop, J. M. Meijer, P. Keim, C. M. Aegerter, G. J. Aubry, G. Maret, *Adv. Opt. Mater.* **2019**, *7*, 1900442; c) E. S. A. Goerlitzer, R. N. Klupp Taylor, N. Vogel, *Adv. Mater.* **2018**, *30*, 1706654.

[22] C. E. Finlayson, G. Rosetta, J. J. Baumberg, *Materials.* **2021**, *14*, 5298.

[23] a) S. C. Daminabo, S. Goel, S. A. Grammatikos, H. Y. Nezhad, V. K. Thakur, *Mater. Today Chem.* **2020**, *16*, 100248; b) R. Arrigo, A. Frache, *Polymers.* **2022**, *14*, 1754.

[24] 3D-Printy, https://www.thingiverse.com/thing:6234369 (accessed: September 2024).

[25] A. Tesar, https://www.thingiverse.com/thing:4589832 (accessed: September 2024).

[26] Gordyt47, https://www.printables.com/de/model/569151 (accessed: September 2024).

[27] C. G. Schäfer, *Dissertation*, TU Darmstadt, Darmstadt **2016**.